Effect of quantized conductivity on the anomalous photon emission radiated from atomic-size point contacts

Mickaël Buret, Igor Smetanin, Alexander Uskov, Gérard Colas Des Francs, Alexandre Bouhelier

Research article

Mickaël Buret, Igor V. Smetanin, Alexander V. Uskov, Gérard Colas des Francs and Alexandre Bouhelier*

Effect of quantized conductivity on the anomalous photon emission radiated from atomic-size point contacts

https://doi.org/10.1515/nanoph-2019-0325
Received August 23, 2019; revised October 16, 2019; accepted October 20, 2019

Abstract: We observe anomalous visible to near-infrared electromagnetic emission from electrically driven atomic-size point contacts. We show that the number of photons released strongly depends on the quantized conductance steps of the contact. Counterintuitively, the light intensity features an exponential decay dependence with the injected electrical power. We propose an analytical model for the light emission considering an out-of-equilibrium electron distribution. We treat photon emission as a Bremsstrahlung process resulting from hot electrons colliding with the metal boundary, and find qualitative accord with the experimental data.

Keywords: electromigration; point contact; quantized conductivity; visible light emission; Bremsstrahlung.

1 Introduction

An atomic-scale contact formed between two macroscopic metal leads has been a canonical testbed for understanding the quantum nature of electron and heat transport at this ultimate length scale [1, 2]. Central to the discussion is the role of dissipation, which must be taken into account in any finite-conductance, externally driven electrical device. In the phenomenological treatment of quantum transport of a one-dimensional conductor [3, 4], the collision-free transmission imposes the dissipation to occur away from the ballistic channel, i.e. in the reservoirs contacting the conductor in a distance equal to the inelastic electron mean free path. Even when describing electron flow from first-principles quantum kinetics [5], inelastic coupling to the interface region guarantees the conservation of the charge required for any open geometry [6]. It is generally understood that the main channel for energy dissipation in a out-of-equilibrium ballistic contact occurs via a coupling to the vibrational degrees of freedom of the system and the local generation of heat [7]. Population of the phonon distribution has been confirmed through voltage-dependent conductance spectroscopy [8, 9] and weak-field current fluctuations analysis [10, 11].

Such inherent fluctuations of the charge current are necessarily accompanied by the emission of a transverse electromagnetic field. For low driving voltages of a coherent conductor, i.e. in the linear regime, radio frequency photons are indeed emitted by the device and may feature nonclassical statistics depending on the voltage applied [12, 13] and the temperature [14]. This was experimentally measured on tunnel junctions at cryogenic temperature and emitting in the gigahertz (GHz) frequency range [15, 16]. For larger driving biases, the situation becomes complicated and the standard fluctuation-dissipation theory is no longer applicable [17, 18]. Electron-electron scattering must be included in the dissipation, as it contributes to the elevatation of the temperature of the Fermi-Dirac distribution. In turn, the electron and the phonon subsystems are not longer thermalized [19–22].

In this work, we identify the presence of a corollary dissipation mechanism. We show that the high-temperature nonequilibrium electron gas formed in an externally driven atomic-scale contact dissipates energy by emitting electromagnetic radiation tailing in the visible part of the spectrum. We observe an increase of the photon rate every time a transmission channel governing the electronic

*Corresponding author: Alexandre Bouhelier, Laboratoire Interdisciplinaire Carnot de Bourgogne CNRS UMR 6303, Université de Bourgogne Franche-Comté, 21000 Dijon, France, e-mail: alexandre.bouhelier@u-bourgogne.fr. https://orcid.org/0000-0002-0391-2836
Mickaël Buret and Gérard Colas des Francs: Laboratoire Interdisciplinaire Carnot de Bourgogne CNRS UMR 6303, Université de Bourgogne Franche-Comté, 21000 Dijon, France
Igor V. Smetanin and Alexander V. Uskov: Lebedev Physical Institute, Leninsky pr. 53, 119991 Moscow, Russia

transport closes. Opposite to the conventional exchange of energy to a thermal bath and to standard electroluminescence, the light intensity emitted by the contact inversely scales with the electrical power dissipated nearby the ballistic conductor. We treat the emission of photons by as spontaneous Bremsstrahlung radiation emerging when hot electrons collide with the metal wall to explain the experimental results.

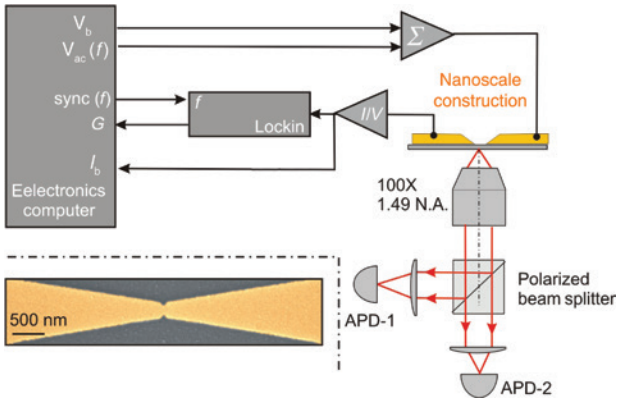

Figure 1: Experimental setup used for measuring simultaneously electron transport and light emission during the electromigration of a Au constriction shown in the inset.
The electromigration is facilitated by controlling the voltage applied to the constriction. The latter is the sum of a d.c. contribution (V_b) and an a.c. one (V_{ac}) oscillating at a frequency f. A current-to-voltage converter (I/V) provides a measure of the current flowing in the constriction (I_b). The conductance (G) of the device is extracted by lock-in detection at f, and the photons are collected by a high-numerical-aperture objective and measured with two cross-polarized avalanche photodiodes (APD-1, APD-2).

2 Experimental methodology

2.1 Sample fabrication

In this work, atomic-size electron channels are formed by electromigrating Au constrictions [23] placed on a glass substrate. The constrictions have typically a bow tie-like geometry with a neck width of approximately 150 nm. These constrictions are fabricated by standard electron beam lithography followed by successive thermal evaporations of a thin layer of Cr and a 50-nm-thick layer of Au. The 3-nm-thick Cr layer improves the adhesion of gold to the glass. The macroscopic Au leads making electrical contacts to both ends of the constriction are realized by optical ultraviolet lithography. A scanning electron micrograph of a pristine constriction is displayed in the inset of Figure 1.

2.2 Electrical controls

Electromigration of the constriction is carried out at ambiant conditions. We apply a variable voltage source V_b along with a 20 mV alternative voltage V_{ac} oscillating at frequency $f = 12.1$ kHz. V_{ac} is used to extract the conductance G of the device with lock-in detection (HF2LI Zurich Instrument). $G = \frac{\partial I_{ac}}{\partial V_{ac}}$, where I_{ac} is the component of the electrical current oscillating at f flowing in the constriction and measured by a current-to-voltage amplifier (I/V DLCPA-100 Femto GmBH; gain $= 10^2$ V/A; load impedance $= 50$ Ω). The layout of the experiment is depicted in Figure 1, where the signal generation and detection is performed by a scanning electronics system (R9 RHK Technology). The total resistance of the electric circuit is roughly 500 Ω and may vary from sample to sample. The resistances of the contacts, the electrical cable, and the measurement device contribute ~470 Ω. The constriction's resistance before electromigration is thus a few tens of ohms. When increasing the voltage V_b above the onset of electromigration, a drop in conductance signals the reorganization of the morphology of the conductor. A larger fraction of the applied voltage is dropped of the constriction when it starts to thin down, and the process enters an active phase. Typically, this regime starts when the total resistance is ~1 k Ω in our circuitry, but the exact value depends on the series resistance [24]. If uncontrolled, this eventually leads to a thermal runaway and a catastrophic rupture of the constriction [25]. Instead, if V_b is decreased to contain the time evolution of the conductance, the electromigration process slows down, allowing us to explore the various regimes of electron transport ranging from diffusive to ballistic, and eventually tunnel when the last atomic bond breaks [26]. Quantized steps of the conductance in units of the quantum of conductance $G_0 = 2e^2/h$ are the signature of a ballistic transport, where e is the electron charge and h is the Planck constant [27, 28].

2.3 Optical interrogations

We align the constriction to the focus of an inverted optical microscope (Nikon Eclipse) equipped with a high-numerical-aperture (NA) objective (NA = 1.49). We detect the light activity during the electromigration process by capturing the photon emission with two single-photon-counting avalanche photodiodes (APD; SPCM-AQR, Perkin Elmer). The quantum efficiency of the APDs sets the detected spectral range to photon energies spanning the visible and

near-infrared region (ca. 1.2–3.1 eV). We use a cross-polarized detection scheme to discriminate photons with an electric field aligned with the main axis of the geometry from those emitted with a transverse polarization state, an expected signature from surface-plasmon-mediated emission of such biased nanoscale contact [29]. All experiments are performed at room temperature in a laboratory environment.

3 Experimental results

3.1 Time traces

Figure 2 shows examples of the time traces recorded at the end of the electromigration process taken before and after the electrical failure of two different devices. Both time traces display the simultaneous dynamics of the normalized conductance (right axis) and the photon counts (left axis). The applied voltage is maintained constant at $V_b = 800$ mV in (A) and $V_b = 700$ mV in (B). The time bin of the acquistion is 10 ms. The step-like evolution of the normalized conductance G/G_0 suggests that the devices undergo a change of the transport mechanism from ballistic to tunnel; the abrupt passage takes place at $t = 27.8$ s in Figure 2A and at $t = 64.2$ s in Figure 2B. The plateaus in the normalized conductance are consistent with numerous observations reported in the past [24, 25, 27, 28]. There is evidence of sub-quantum steps, especially in the regime where the conductance explores values between $6G_0$ and $4G_0$. These noninteger excursions have already been reported in gold contacts [30, 31]. They are linked to the atomic rearrangement of the contact [32, 33] and can be understood from quantized conductors placed in series [34]. In the time traces displayed in Figure 2, the amplitudes of the voltage applied during the last moment reduce the probability of G to explore the smallest integer numbers $N \times G_0$ [35], and the last measured step is at approximately $N = 4$ in both cases. We have observed lower quantum numbers in the past [26, 36], but typically with applied voltage before rupture below 500 mV.

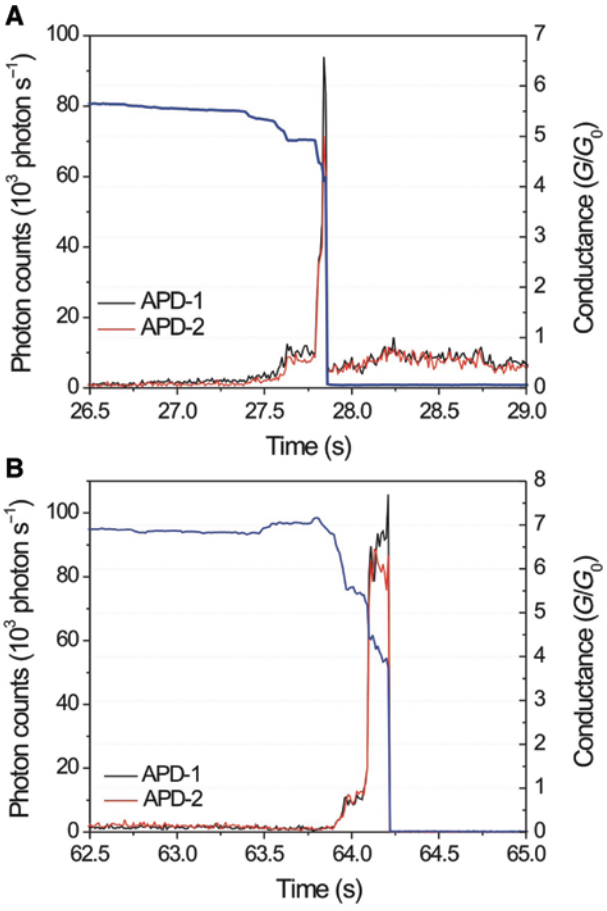

Figure 2: Photon counts and measured conductance versus time. (A, B) Conductance (normalized) and photon counts time traces captured during the last moment of electromigration for two different devices. The rupture occurs at $t = 27.8$ s in (A) and at $t = 64.2$ s in (B). The conductance is normalized by the quantum of conductance G_0. Stepwise closing of conduction channels in approximate units of G_0 is correlated with an increase in photon emission. The cross-polarized APD-1 and APD-2 share similar trends.

Figure 2 also displays the simultaneously acquired photon counts measured by the two cross-polarized APDs. In this detected range of counts, the APD counting modules are linear. The graphs show an unambiguous correlation between the conductance steps and light emission. Photons emitted in the detected spectral window are measured as soon as $G \sim 5G_0$, with a rate staying constant for the duration of the conductance plateaus. A tenfold increase of the number of photons is concomitant to the closing of an electron transmission channel identified by the short excursion of G at $4G_0$ in both examples.

Immediately after the rupture of the device, electron transport occurs by tunneling and the junction features conductances of $G = 6 \times 10^{-3} G_0$ and $G = 1.4 \times 10^{-3} G_0$, measured at $V_b = 800$ mV and $V_b = 700$ mV, respectively. In both cases, the photon rate drops when electron transport changes from ballistic to tunnel. Light emission is still observed in this tunneling regime with the junction of Figure 2A.

3.2 Discussion about the mechanisms of light emission

Light emitted by tunnel junctions has been a subject of intense research since Lambe and McCarthy identified

the crucial role of inelastic electron coupling to decaying surface plasmons [37]. In the latest advances, tunnel junctions are constituting the active feed of the next generation of electrically driven optical antennas [36, 38–40]. In this context, engineering the surface plasmon landscape and the barrier height is expected to boost the notoriously low transduction yield plaguing inelastic energy transfer [41–43]. Continuing on this, a recent proposal suggested that multiple collisions of transported electrons with the boundaries of a plasmonic ballistic constriction may significantly improve the probability to generate an electromagnetic response [29].

During the entire time traces and the excursion of G in the different transport regimes, the photon energy is always greater than the bias energy. The quantum inequality $h\nu \leq eV_b$ is systematically violated, where ν is the frequency of the photon. We can thus exclude emission processes akin to inelastic tunneling [44] to explain the light activity. This is further confirmed by the similarity of the signals detected by the two cross-polarized APDs. Inelastic coupling to surface plasmon modes in the metallic contact is expected to show a polarization anistropy [29, 39]. As shown in the time traces of Figure 2, this particular radiative pathway triggered by the decay of surface plasmons is not observed experimentally either in the regime of quantized conduction steps or when the electrons are tunneling. The two cross-polarized signals are at the same count level at all times. Such unpolarized light in the regime of overbias emission confirms our earlier measurement performed with tunnel devices [36], where a wavevector analysis did not show evidence of running surface plasmon. The spatially extended geometrical system introduced by the electrical leads further contributes to the absence of well-defined local surface plasmon resonance.

3.2.1 Tunnel regime: light emission after the rupture

Considering that $h\nu \geq eV_b$, the emission released in the regime of electron tunneling for $t \geq 27.8$ s in Figure 2A is due either to the radiative glow of a hot electron distribution [36, 45] or to higher order electron-plasmon interactions [46–49]. The fast dynamics of the last moment of electromigration prevents us from acquiring information pertaining to the spectral content of the light, which would have been instrumental for discriminating the physical origin of the light emitted in the regime of electron tunneling. For the second device, the smaller applied bias combined with a lower conductance inhibits the emission, if any, to the tail in the detected energy window.

3.2.2 Ballistic regime: light emission before the rupture

The range of conductance values explored here (a few G_0) before the tunnel barrier forms is similar to that in the work of Malinowski et al., where infrared emission interpreted as blackbody radiation of an out-of-equilibrium electron gas was measured in mechanically controlled break junctions [45]. Figure 3A is a semilogarithmic plot displaying the dependence of the total photon counts (sum of the two APDs) versus conductance gathered from nine electromigrated devices. The red circles and the light blue diamonds are the experimental points inferred from Figure 2A and B, respectively. The evolution with conductance is consistent across the tested devices: light emission is detected when the conductance of the contact enters $8G_0$ to $5G_0$ and dramatically increases up to the breaking

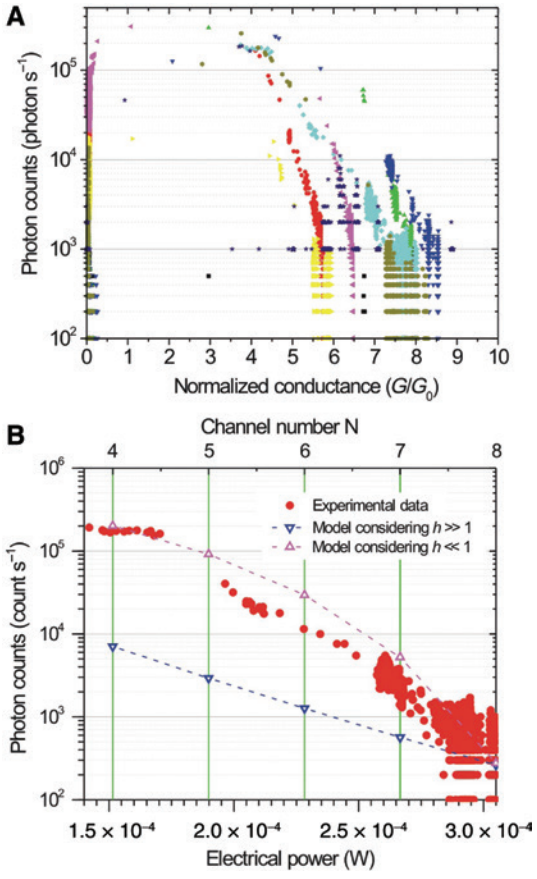

Figure 3: Photo counts versus conductance and electrical power. (A) Concatenation of results obtained on nine devices showing the evolution of the photon counts (logarithmic scale) with the normalized conductance. The dark count rate of the APDs is about 300 counts s^{-1}. (B) Semilogarithmic plot of the photon count dependence on the dissipated power $P = I_b^2 \times G^{-1}$ in the contact ($V_b = 700$ mV). The magenta and the blue inverted triangles are the model expectation, considering either a vanishing heat exchange at the side wall ($h \ll 1$) or an efficient thermalization ($h \gg 1$), respectively.

point characterized by $G < G_0$. Even in the absence of well-defined quantized steps in the conductance trace, anomalous photon emission from the constriction can be linked to an indirect demonstration of ballistic electron transport in the system.

The few data points between $4G_0$ and G_0 suggest that the light emission levels off. However, the rapid failure of the contact during the last moment of the electromigration process prevents us from making an affirmative statement. Like the junction displayed in Figure 2A, some devices are optically active in the tunneling regime, as shown by the data points located below G_0 in Figure 3A.

Early observations of overbias emission in an atomic contact have shown that it follows a power-law relationship with the electrical power injected in the device. For a given value of the conductance, and regardless of the emission mechanism at play, increasing the current by changing the electrical bias drastically boosts the detected photon counts [45, 46]. In the present experiment, the voltage bias is maintained at a constant value during the last moment of electromigration. The excursion of the conductance in the ballistic regime allows us to monitor the evolution of the photon counts with the electrical power dissipated in the contact without changing the driving conditions and to obtain a deeper insight into the emission mechanism. Light is emitted when the conductance of the contact reaches $5G_0$, i.e. ~2.5 kΩ. Considering a series resistance of 470 Ω, about 85% of the voltage drop occurs at the constriction. At $4G_0$, it is 87% of the bias, which is falling. The small difference in the voltage applied cannot account for the one order of magnitude difference of the detected photon counts. Furthermore, the voltage drop is maximum when the contact between the two leads is broken. In this regime of largest potential drop, light emission is either weak or absent in the time traces of Figure 2. For low driving voltages, the process responsible for light emission remains modest and its spectral tail in the visible cannot be discriminated from the background noise. Thus, a trade-off exists between the probability of G to explore few G_0 and detecting an overbias light activity. Here, at 700 mV bias, the smallest integer is $N = 4$. When the transport channels are closing, the electrical power dissipated in the contact reduces concomitantly. Figure 3B shows a semilogarithmic plot of the measured light intensity (red circles) versus the electrical power P inferred from Figure 2A before the electrical failure using the relation $P = I_b^2 \times G^{-1}$, where I_b is the current flowing through the contact. The graphs unequivocally demonstrate that the photon count is maximum at lower electrical power and features an exponential decay with P. This trend is opposite to measurements performed at constant G [45, 46].

4 Analytical model

4.1 Working hypothesis

In the following, we develop a theoretical framework to understand the relationship between the number of channels opened for electron transmission and the optical activity emitted at an overbias photon energy. The delivered electric power scales with the number of transport channels N as $P_N = V_b^2 N G_0$. The radius of the Nth channel can be estimated as $r_N \approx N r_1$. Here, $r_1 \approx \lambda_F/4$ is the characteristic radius of the first quantum channel [3] and λ_F is the Fermi wavelength of the ballistic electrons. As a result, both the current density and the power density are increasing in proportion to $1/N$ when the transport channels are closing. Thus, increasing the dissipated power results in a rise of the peak electron temperature within an area located at the end of the transport channel. Photons may be emitted by such a nonequilibrium distribution if electrons interact with the surface [19]. Qualitatively, this is expected to be the origin of the measured increase in photon yield at energies higher than the bias when the constriction explores the lower values of conductance quanta.

4.2 Model of nonequilibrium electron temperature distribution

Below, we present a qualitative model that illustrates the above consideration. We assume that the electric current is transported by a channel connected to the drain contact through an interconnection region, which we model by a cylinder of radius R_0 and finite length L_c, as schematically shown in Figure 4. The electron subsystem in this interconnection region is out of equilibrium because of the fast heating due to the arriving and colliding quasi-ballistic electrons. We assume a local temperature T_e for the

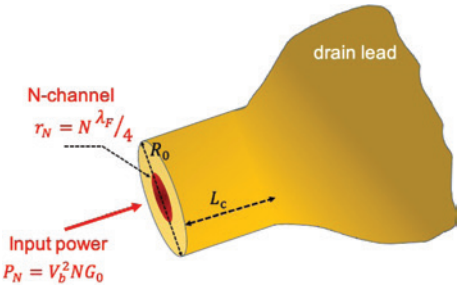

Figure 4: Sketch representing the constriction and the different characteristic parameters used in the model.

electrons well above the homogeneous lattice temperature T_L. The reader is referred to Ref. [22] for an exhaustive discussion on the temperature of the electronic distribution in driven nonequilibrium nanoscale constrictions. We treat the heat transport problem in this interconnection region in the frame of the two-temperature model, assuming that the lattice temperature T_L does not change significantly along the interconnection region.

4.2.1 Electron temperature

In accordance with the experimental conditions, we will seek a steady-state temperature distribution

$$C_e \frac{\partial T_e}{\partial t} = \nabla(\kappa_e \nabla T_e) - g(T_e - T_L) = 0, \quad (1)$$

where g is the electron-lattice coupling constant, κ_e is the electron thermal conductivity, and C_e is the electron heat capacity. At electron temperatures below the Fermi temperature $T_e \le T_F$, the electron thermal conductivity is given by $\kappa_e = C_e v_F^2 \tau / 3$, where v_F is the Fermi velocity and τ is the characteristic electron transport relaxation time. In a bulk metal, τ is determined by the electron-phonon and the electron-electron collisions: $1/\tau = 1/\tau_{e\text{–}ph} + 1/\tau_{e\text{–}e}$ [50, 51]. When the lattice temperature exceeds the Debye temperature, the electron-phonon collision rate can be estimated as $1/\tau_{e\text{–}ph} \sim k_B T_L/\hbar$ so that at room temperature we find $\tau_{e\text{–}ph} \sim 30$ fs. Electron-electron collisions dominate at electron temperatures exceeding $T_e \ge T_* \sim (E_F T_L/k_B)^{1/2}$, so one can find for gold $T_* \approx 4 \times 10^3$ K, where E_F is the Fermi energy and k_B is the Boltzmann constant. In the case of our interest, the actual size of the interconnection region is much smaller than the mean free path of an electron in the bulk material. The characteristic electron transport relaxation is determined rather by collisions with the walls of the interconnection region, and we can use the following estimate $\tau \sim R_0/v_F$. As a result, the electron thermal conductivity in the interconnection region is much smaller than that for the bulk material, which provides a large difference between the lattice temperature and the temperature of quasi-ballistic electrons. We will show below that it explains qualitatively our anomalous experimental dependences of the above-voltage photon yield on the electric power delivered in the contact.

With the above estimate, the electron thermal conductivity coefficient scales linearly with the electron temperature: $\kappa_e \equiv \kappa_e(T_e) = b \times T_e$, with the proportionality coefficient $b = \pi^2 v_F^2 \tau N_e k_B^2 / 6E_F$ and N_e is the number of electrons. The electron-lattice coupling constant g can be estimated through the heat capacity of electrons: $C_e = C_e' T_e = (\pi^2 N_e k_B^2 / 2E_F) T_e$ and thus also scales linearly with T_e, $g \sim C_e/\tau_{e\text{–}l} = (C_e'/\tau_{e\text{–}l}) T_e$. Here, $\tau_{e\text{–}l}$ is the characteristic timescale for the electron-lattice energy transfer. Keeping in mind these scaling dependences, we can rewrite the electron temperature conduction equation as $\Delta T_e^2 - T_e^2/L_0^2 \approx 0$, with the characteristic length $L_0 = (v_F^2 \tau_{e\text{–}l} \tau/6)^{1/2} \approx (R_0 v_F \tau_{e\text{–}l}/3)^{1/2}$.

As the natural boundary conditions, we assume the electron temperature in the drain electrode far from the contact to be at the equilibrium with the lattice temperature, so that $T_e(z = L_c) = T_L$. At the front end of the contact, $z = 0$ (the z-axis is along the cylinder axis connecting the drain electrode), the electric power is assumed to be homogeneously deposited in a spot with radius r_N of opened quantum transport channels N, so that the boundary heat flux is $\kappa_e(\partial T_e/\partial z)_{z=0} = -p_N \Theta(r - r_N)$, $p_N = P_N/\pi r_N^2 = (G_0 V_b^2/\pi r_1^2) N^{-1}$, and $\Theta(x)$ is the step function defined as $\Theta(x > 0) = 0$ and $\Theta(x < 0) = 1$.

At the side wall of the cylinder $r = R_0$, we assume that the heat flux is determined by the energy loss of the electrons in collision with the metal boundary, in analogy with the Fedorovich-Tomchuk mechanism [52]. In this framework, the heat flux at the side wall is proportional to the squared temperature: $\kappa_e(\partial T_e/\partial r) = -B(T_e^2 - T_L^2)$. Here, B is a proportionality coefficient. As far as $\kappa_e = b \times T_e$, we find $(b/2)(\partial T_e^2/\partial r) = -B(T_e^2 - T_L^2)$. Finally, we set $h = 2BR_0/b$ and find $\partial T_e^2/\partial r + (T_e^2 - T_L^2)h/R_0 = 0$, with h being a dimensionless parameter characterizing the electron energy exchange rate at the side wall. The limit $h = 0$ corresponds to zero heat flux at the side wall and $\partial T_e^2/\partial r$ vanishes. Large values of the parameter $h \gg 1$ describe a fast energy exchange, leading to the rapid establishment of equilibrium between the electrons and phonons, i.e. $T_e = T_L$.

Under the above assumptions, the steady-state temperature distribution can be written as

$$T_e^2 = T_L^2 + T_0^2 \sum_{n=0}^{+\infty} a_n J_0(\mu_n r/R_0) \sinh(\lambda_n (L_c - z)/R_0) \quad (2)$$

The coefficients a_n are given by

$$a_n = \frac{\mu_n J_1(\mu_n \zeta_N)}{\lambda_n \mu_n^2 ([J_1(\mu_n)]^2 + [J_0(\mu_n)]^2)} \frac{1}{\cosh(\lambda_n L_c/R_0)} = \frac{\mu_n J_1(\mu_n \zeta_N)}{\lambda_n (\mu_n^2 + h^2)[J_0(\mu_n)]^2} \frac{1}{\cosh(\lambda_n L_c/R_0)} \quad (3)$$

Here, $\zeta_N = r_N/R_0$, μ_n is the root of the equation $\mu_n J_1(\mu_n)/J_0(\mu_n) = h$ with $n = 0, 1, 2, \ldots$, and the eigen values of the problem along the z-axis are $\lambda_n = (\mu_n^2 + R_0^2/L_0^2)^{1/2}$. The coefficient T_0^2 before the sign of the sum in

Eq. (2) does not depend on the channel's number, $k_B^2 T_0^2 = 96(eV_b)^2 E_F / \pi^4 \hbar N_e v_F^2 \lambda_F \tau$. Within the accepted above approximation for the electron transport relaxation time, $\tau \sim R_0/v_F$, using the well-known relation $N_e = k_F^3/3\pi^2$, we find $k_B T_0 = (6/\pi^2)(eV_b)(\lambda_F/R_0)^{1/2}$, which for the applied voltage $V_b = 0.7$ V results in $T_0[10^3\ \mathrm{K}] \approx 4.92\sqrt{\lambda_F/R_0}$.

4.2.2 Dependence of T_e on the number of transport channels

According to Eq. (2), the maximum temperature is at the center of a hot spot situated at the front end of the cylinder ($z=0$, $r=0$). When the side wall heat transfer is fast, i.e. the coefficient h is large ($h \to +\infty$), the boundary condition reads $T_e(r=R_0) = T_L$, and $\mu_n \to \mu_n'$ becomes zeros of the Bessel function $J_0(\mu_n') = 0$ with $n = 1, 2\ldots$. The value of the characteristic length L_0 well exceeds R_0, $L_0/R_0 \approx (v_F \tau_{e-l}/3R_0)^{1/2} \gg 1$. Thus $\lambda_n \approx \mu_n'$, and the maximum temperature in this limiting case is

$$T^2_{e[h\to+\infty]} \approx T_L^2 + T_0^2 \sum_{n=0}^{+\infty} \frac{J_1(\mu_n' \zeta_N)}{[\mu_n' J_1(\mu_n')]^2} \tanh\left(\frac{\mu_n' L_c}{R_0}\right). \qquad (4)$$

In the opposite case of vanishing energy exchange at the side wall, i.e. $h \ll 1$ or even $h = 0$, the roots $\mu_n \to \mu_n''$ consist in the zeroth root $\mu_0'' \approx \sqrt{2h}$ (for which the corresponding eigen value is $\lambda_0 \approx (2h + R_0^2/L_0^2)^{1/2} \to R_0/L_0$), and the sequence of the roots of the first-order Bessel function $J_1(\mu_n'') \approx 0$, with $n = 1, 2\ldots$, and the maximum temperature can be estimated as

$$T^2_{e[h\to 0]} \approx T_L^2 + T_0^2 \left[\frac{\zeta_N L_c}{R_0} + \sum_{n=0}^{+\infty} \frac{J_1(\mu_n'' \zeta_N)}{[\mu_n'' J_0(\mu_n'')]^2} \tanh\left(\frac{\mu_n'' L_c}{R_0}\right)\right]. \qquad (5)$$

The dependence of the maximum electron temperature versus the number of quantum transport channels is shown in Figure 5A and B for both limiting cases ($h \ll 1$ and $h \gg 1$) and gradually increasing length L_c of the cylinder interconnection region. The radius of the cylinder is fixed at $R_0 = 2.5\lambda_F$, which corresponds to a maximum of 10 available quantum channels in the contact. For each channel number N, the peak temperature increases with an increase in the cylinder length L_c ranging from $L_c = R_0/6$ to $L_c = R_0$. Obviously, the largest electron temperature is attained when the exchange rate at the side wall is weak ($h \ll 1$). We can draw the first important counterintuitive conclusion: regardless of the mechanism dictating the inelastic energy loss at the wall of the constriction, the electronic temperature drops with increasing electrical power dissipation (large N). This dependence is more

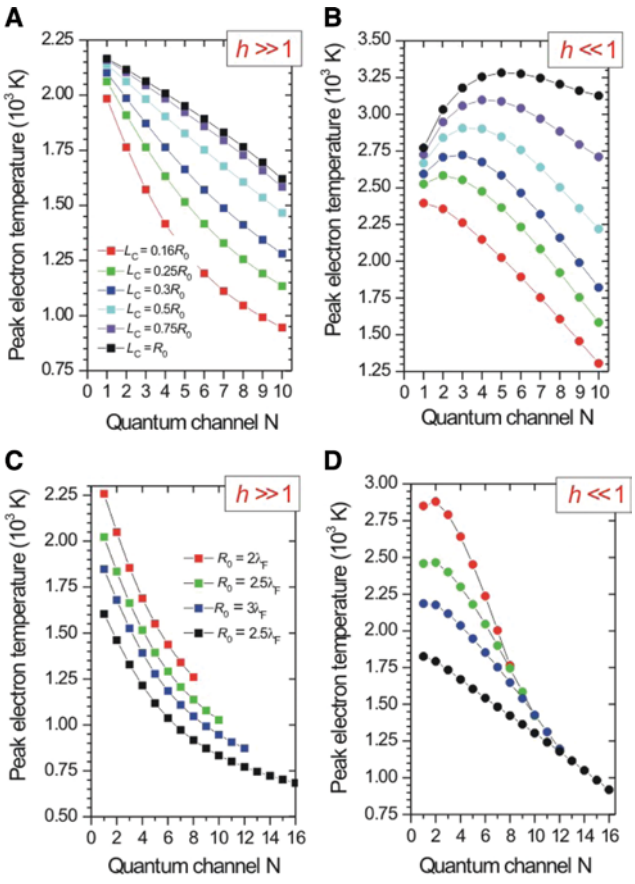

Figure 5: Peak electron temperature versus the number of open quantum channels N in the contact calculated in (A) and (B) at a fixed radius $R_0 = 2.5\lambda_F$, and in (C) and (D) at a fixed cylinder length $L_c = \lambda_F/2$.
Squares represent data at large parameter $h \gg 1$, while circles correspond to $h \ll 1$. In (A) and (B), data are plotted for different lengths of the interconnection region: $L_c = R_0/6$ (red), $L_c = R_0/4$ (green), $L_c = R_0/3$ (blue), $L_c = R_0/2$ (cyan), $L_c = 3R_0/4$ (violet), and $L_c = R_0$ (black). In (C) and (D), the data are plotted for different radii of the cylinder interconnection region: $R_0 = 2\lambda_F$ (red), $R_0 = 2.5\lambda_F$ (green), $R_0 = 3\lambda_F$ (blue), and $R_0 = 4\lambda_F$ (black).

pronounced for short lengths of the interconnection region when the side wall energy exchange is efficient ($h \gg 1$). In the other limiting case ($h \ll 1$), a change in the trend appears with increasing L_c, with the occurrence of a maximum shift to higher N. This is the consequence of the first term in brackets in the right-hand side of Eq. (5), which grows linearly with N. In turn, at sufficiently large L_c, the peak temperature will start increasing with N before decreasing. This can be understood from the following argument:

In the case of small h, heat is only exchanged at the distal end of the interconnection, and if the length is sufficiently large, all the transverse oscillations exponentially vanish according to Eq. (5) except the constant flow

(corresponding to the lowest eigen value), which is proportional to the injected power.

Figure 5C,D displays the dependence of the maximum electron temperature versus the number of quantum transport channels at the fixed length $L_c = R_0/3$ and various radii R_0 ranging from $R_0 = 2\lambda_F$ (8 quantum channels available) to $R_0 = 4\lambda_F$ (16 quantum channels available). The dependences are more pronounced when $h \ll 1$ and for smaller radii and become smoother with increase in R_0.

Since the electrical power dissipated in the contact areas scales with N ($P_N = V_b^2 G_0 N$), Figure 5 agrees with experimental trend of Figure 3B providing we can link the electron temperature T_e to the number of photons emitted by the contact.

4.3 Bremsstrahlung emission emerging from nonequilibrium hot electrons colliding with the metal boundary

In a bulk metal, hot nonequilibrium electrons lose their energy mostly during nonradiative collisions with phonons or impurity atoms. Primary photons are emitted as a result of the corresponding Bremsstrahlung processes (at temperatures of our interest, one can omit photons emitted in bound-bound transitions in lattice atoms). Establishment of thermal equilibrium of photons is the consequence of complicated kinetics of free-free electron transitions consisting in emission and absorption Bremsstrahlung processes as well as the Compton effect [53, 54]. In a simplified diffusion approximation, photon emission can be treated through the radiation transfer equation

$$\frac{dI_\omega}{ds} = -\alpha_\omega I_\omega + \alpha_\omega B_\omega(T_e), \tag{6}$$

where I_ω is the radiation intensity spectrum, α_ω is the absorption coefficient at the given frequency, and $B_\omega(T_e)$ is the equilibrium radiation intensity given by Planck's law. In a bulk metal, when the optical skin depth α_ω^{-1} is much smaller than the characteristic dimension, Eq. (6) results in Kirchhoff's law, and the emissivity is given by $j_\omega = \alpha_\omega B_\omega(T_e)$.

In the case of a small interconnection region near the constriction, the region of elevated electron temperature is given by $r_N \approx N\lambda_F/4$ and is much smaller than the optical skin depth α_ω^{-1}. As a result, an equilibrium photon distribution cannot be established within the interconnection region and Kirchhoff's law is no longer valid. Consequently, the emission of photons is primarily guided by a thermal Bremsstrahlung process. Hot electrons in the interconnection region are quasiballistic: the electron-phonon mean-free path is measured as $l_{e-ph} = v_F \tau_{e-ph} \sim 60$ nm for Au [55]. Digressing from the presence of impurities and from the two-photon Compton emission in electron-electron collisions, we conclude that the optical activity detected in our experiment is mainly due to a Bremsstrahlung process resulting from hot electrons colliding with the surface potential. We note that within the detected spectral range, a spontaneous emission of an elevated electron temperature discussed in Refs. [36, 45] cannot be distinguished from thermal Bremsstrahlung, as both processes share the same wavelength dependence [56].

To find the photon yield in the electron-wall Bremsstrahlung radiation process, we utilize the conventional quantum mechanical calculation technique, which is analogous to that used in the theory of size-dependent conductivity of thin metal films by Trivedi and Ashcroft [57] as well as in the theory of intersubband transitions in semiconductor quantum wells [58, 59]. We consider a metal slab of the thickness L, which is considered to be sufficiently large to provide limiting transition to the continuous spectrum of electron momentum. Let the coordinate axis z be transverse to the slab boundary and $\vec{\rho}$ be the coordinate in the boundary plane. The wall of the slab, at $z = 0$, L, is modeled by an infinite stepwise potential. Within the jellium model of a noninteracting electron system, the wavefunction of an electron inside the slab is

$$\Psi(z, \vec{\rho}, t) = \sqrt{\frac{2}{V_e}} \sin[k_z z] \exp(i\vec{k}_\perp \vec{\rho}) \exp\left(-i\frac{\varepsilon}{\hbar}t\right), \tag{7}$$

which satisfies the boundary conditions $\Psi(z=0) = \Psi(z=L) = 0$, $k_z = (\pi/L)j$, $j = 1, 2, 3\ldots$, is the longitudinal wavenumber, $\hbar\vec{k}_\perp$ is the transverse momentum, and V_e is the quantization volume for the electron. The energy of electrons $\varepsilon = (\hbar^2/2m)(k_z^2 + |k_\perp|^2)$ is the eigen value of the unperturbed Hamiltonian, the perturbation Hamiltonian $H_{int} = -(e/mc)\hat{\vec{A}}\hat{\vec{p}}$, $\hat{\vec{p}} = -i\hbar\nabla$, describes the spontaneous photon emission in a given mode of the wavevector $\vec{k}$, the polarization σ, and the frequency $\omega = |\vec{k}|c$, with the following vector potential:

$$\hat{\vec{A}} = \left(\frac{2\pi\hbar c}{V_{ph}\omega}\right)^{1/2} \hat{a}^+_{\vec{k},\sigma} \vec{e}^{\,\star}_{\vec{k},\sigma} \exp(-i\vec{k}\vec{r}) e^{-i\omega t}. \tag{8}$$

Here, $\hat{a}^+_{\vec{k},\sigma}$ is the corresponding photon creation operator, $\vec{e}^{\,\star}_{\vec{k},\sigma}$ is the unit polarization vector, and V_{ph} is the quantization volume for photons. Transitions are induced between the initial state $|i\rangle$ of an elecron with the energy

ε_i and empty photon state and the final state $|f\rangle$ of electron with energy ε_f and one photon of the above mode. The rate of transition is given by first-order perturbation theory

$$W_{i\to f}=\frac{2\pi}{\hbar}|\langle f|H_{\rm int}|i\rangle|^2\,\delta(\varepsilon_f-\varepsilon_i+\hbar\omega)d\rho_f. \tag{9}$$

Here, $d\rho_f$ is the number density of the final states, $d\rho_f=(V_{\rm e}/(2\pi)^3)d^3\vec{k}_f\times(2V_{\rm ph}/(2\pi)^3)d^3\vec{k}$, in the limit of continuous states. The matrix element can be easily calculated as follows:

$$\langle f|H_{\rm int}|i\rangle=i\frac{4e\hbar}{mV_{\rm e}}\left(\frac{2\pi\hbar c}{V_{\rm ph}\omega}\right)^{1/2}\times\frac{k_{i,z}k_{f,z}}{k_{i,z}^2-k_{f,z}^2}(\vec{e}^{\,*}_{\vec{k},\sigma},\vec{e}_z)\delta(\vec{k}_{i,\perp}-\vec{k}_{f,\perp}). \tag{10}$$

Here, $\vec{e}_z$ is the unit vector along the z-axis. The delta function in the matrix element [Eq. (10)] demonstrates the conservation of the transverse (parallel to the wall) component of the electron momentum, while its z-component changes according to the energy conservation law corresponding to the delta function in the right-hand side of the golden rule [Eq. (9)]. To find the spectrum rate of photon emission by a single electron, we have to sum over all the final electron states as well as over the polarization and solid angles of photon emission. The sum over the electron final states in the continuous limit $L\to\infty$ is provided through the following relation:

$$\int\frac{k_{i,z}^2k_{f,z}^2}{(k_{i,z}^2-k_{f,z}^2)^2}\delta^2(\vec{k}_{i,\perp}-\vec{k}_{f,\perp})\times\delta(\varepsilon_f-\varepsilon_i+\hbar\omega)d^3\vec{k}_f =(2\pi)^2S_\perp\frac{m^2v_{i,z}^2v_{f,z}}{4\hbar^3\omega^2}, \tag{11}$$

where $S_\perp$ is the square of the wall boundary, and the velocities $v_{i,z}=\hbar k_{i,z}/m$ and $v_{f,z}=(v_{i,z}^2-2\hbar\omega/m)^{1/2}$ are introduced. The sum over the polarization of Bremsstrahlung photons can be accounted through the substitution $2|(\vec{e}^{\,*}_{\vec{k},\sigma},\vec{e}_z)|^2\to\sin^2\theta$, and after summation over the photon solid angle $d\Omega=\sin\theta d\theta d\phi$, we arrive at the following relation for the Bremsstrahlung emission rate per unit frequency range:

$$\frac{dN_i(\omega)}{d\omega\,dt}=\frac{8e^2v_{i,z}^2v_{f,z}}{3\pi V_{\rm e}\hbar\omega c^3}S_\perp. \tag{12}$$

Let n_i be the number density of electrons with the longitudinal component of velocity $v_{i,z}$; the rate of collisions with the left wall of the metal slab is $\frac{1}{2}n_iS_\perp v_{i,z}$ and the same value holds for the collision rate with the right wall of the slab. Consequently, the total emitted power spectrum per electron ($n_i=1/V_{\rm e}$) is

$$\frac{dP_\omega}{d\omega}=\frac{dN_i(\omega)}{d\omega\,dt}\frac{\hbar\omega}{v_{i,z}S_\perp/V_{\rm e}}=\frac{8e^2}{3\pi c^3}v_{i,z}v_{f,z}. \tag{13}$$

In the classical limit $\hbar\omega\to0$, i.e. when the energy of scattered electron does not change significantly, one can replace $4v_{i,z}v_{f,z}\approx(v_{i,z}+v_{f,z})^2=|\vec{v}_i-\vec{v}_f|^2$ and arrive at the well-known classical relation $dP_\omega/d\omega=(2e^2/3\pi c^3)|\Delta v|^2$ for the power spectrum emitted by scattered electrons [56, 60].

To find the total photon emission rate per unit surface square, we sum Eq. (12) over all the electron states in the slab, assuming the Fermi distribution $f_{\rm F}(\varepsilon)=1/(1+\exp[(\varepsilon-\varepsilon_{\rm F})/k_{\rm B}T_{\rm e}])$.

$$\frac{dN_{\rm ph}(\omega)}{dS\,d\omega\,dt}=\frac{1}{2S_\perp}\int\frac{2d^2\vec{k}_{i,\perp}dk_{i,z}}{(2\pi)^3}V_{\rm e}\frac{dN_i(\omega)}{d\omega}f_{\rm F}(\varepsilon_i)(1-f_{\rm F}(\varepsilon_f)) =\frac{8e^2}{3\pi^3\hbar^3c^3}\frac{k_{\rm B}T_{\rm e}/\hbar\omega}{\exp(\hbar\omega/k_{\rm B}T_{\rm e})-1}F(\omega,T_{\rm e},\varepsilon_{\rm F}), \tag{14}$$

where $\varepsilon_i=(\hbar^2/2m)(k_{i,z}^2+|\vec{k}_{i,\perp}|^2)$, $\varepsilon_f=\varepsilon_i-\hbar\omega$, and the factor $1/2S_\perp$ before the integral takes into account the doubled scattering surface in the slab. The function $F(\omega,T_{\rm e},\varepsilon_{\rm F})$ is given by the following integral:

$$F(\omega,T_{\rm e},\varepsilon_{\rm F})=\int_{\hbar\omega}^{\infty}du\sqrt{u(u-\hbar\omega)} \times\left\{\ln\left[1+\exp\left(\frac{\varepsilon_{\rm F}-u+\hbar\omega}{k_{\rm B}T_{\rm e}}\right)\right]-\ln\left[1+\exp\left(\frac{\varepsilon_{\rm F}-u}{k_{\rm B}T_{\rm e}}\right)\right]\right\}. \tag{15}$$

The total Bremsstrahlung photon number spectrum emission rate given by Eqs. (14) and (15) is a complicated function, which we will analyze in detail elsewhere. To our particular purpose here, we will restrict ourselves by the conditions of our experiment, where the maximum attainable temperature is well below the energy of the collected photons, and we have the following relation between the parameters:

$$k_{\rm B}T_{\rm e}\ll\hbar\omega\ll\varepsilon_{\rm F}. \tag{16}$$

One can easily see that under these conditions, the logarithms in braces in Eq. (15) vanish when the argument exceeds $u>\varepsilon_{\rm F}+\hbar\omega$ and $u>\varepsilon_{\rm F}$, respectively. At $\hbar\omega<u<\varepsilon_{\rm F}$, the term in braces is approximately constant and equals $\hbar\omega/k_{\rm B}T_{\rm e}\gg1$. At $\varepsilon_{\rm F}<u<\varepsilon_{\rm F}+\hbar\omega$, it almost linearly decreases

to zero. As a result, we arrive at the following approximation: $F \approx (\varepsilon_F^2 \hbar\omega / 2k_B T_e)(1 + O(\hbar\omega / \varepsilon_F))$, and finally find

$$\frac{dN_{ph}(\omega)}{dS\, d\omega\, dt} \approx \frac{4e^2\varepsilon_F^2}{3\pi^3\hbar^3c^3} \frac{1}{\exp(\hbar\omega / k_B T_e) - 1}. \quad (17)$$

Compared to the Planck formula for blackbody radiation

$$B_\omega(T_e) = \frac{\omega^2}{2\pi c^2} \frac{1}{\exp(\hbar\omega / k_B T) - 1}, \quad (18)$$

the rate of Bremsstrahlung emission is less by the factor

$$\beta = \frac{8}{3\pi^2} \frac{e^2}{\hbar c} \left(\frac{\varepsilon_F}{\hbar\omega} \right)^2, \quad (19)$$

which under the experimental condition can be estimated to be $\beta \sim 0.1$.

To model the total yield of Bremsstrahlung photons detected in our experiment, we integrate the spectrum rate [Eq. (17)] with the transmission function $Q(\omega)$ of the detection path, which includes the spectral sensitivity of the detector. The APD response restricts the detection efficiency to overbias photon energy tailing in the visible part of the spectrum. We model the spectral response of the APDs by the following function:

$$Q(\omega) \approx \begin{Bmatrix} 0; & \omega < \omega_1 \\ 0.65 \dfrac{\omega - \omega_1}{\omega_2 - \omega_1}; & \omega_2 > \omega > \omega_1 \\ 0.65; & \omega_3 > \omega > \omega_2 \end{Bmatrix}. \quad (20)$$

Here, ω_1 corresponds to the detection threshold of the detector at a wavelength $\lambda_1 = 1070$ nm, ω_2 corresponds to the peak of detection efficiency at $\lambda_2 = 740$ nm, and ω_3 is taken at $\lambda_3 = 600$ nm.

One can easily check that for the domain of interest, i.e. for peak temperatures below 3.5×10^3 K (see Figure 5), the integrated Bremsstrahlung photon yield is well approximated by the relation $dN_{ph}/dSdt \approx 6.13 \times 10^{22} \times \zeta^2 \exp(-1/\zeta) \mathrm{cm}^{-2}\mathrm{s}^{-1}$, where the normalized temperature is $\zeta = k_B T_e / \hbar\omega_1$. The results of our calculation of the Bremsstrahlung photon yield rate dependence on the quantum channel number are shown in Figure 6 both for limiting values of the parameter h governing the heat transfer at the side wall of the system and for varying lengths L_c and radii R_0 of the interconnection region. The data correspond to the calculated peak temperatures shown in Figure 5. One can find that these dependences at

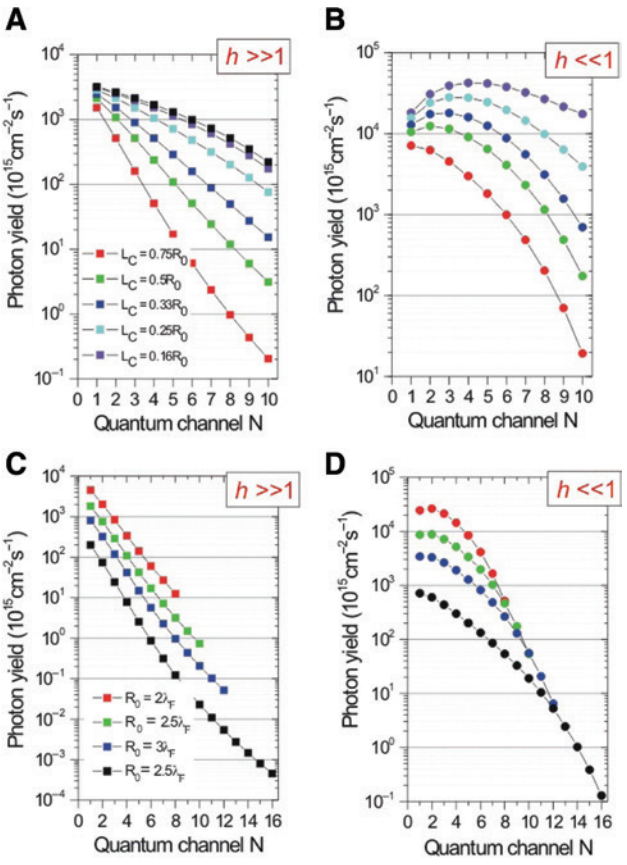

Figure 6: Thermal Bremsstrahlung radiation photon rates versus the number of open quantum channels in the contact.
(A, B) Semilogarithmic plots at a fixed radius $R_0 = 2.5\lambda_F$. Squares represent data at large parameter $h \gg 1$ (A), while circles correspond to $h \ll 1$ (B). Data are plotted at different lengths of the interconnection region: $L_c = R_0/6$ (red), $L_c = R_0/4$ (green), $L_c = R_0/3$ (blue), $L_c = R_0/2$ (cyan), and $L_c = 3R_0/4$ (violet). (C, D) Semilogarithmic plots at fixed cylinder length $L_c = \lambda_F/2$. Data are plotted at different radii of the cylinder interconnection region: $R_0 = 2\lambda_F$ (red), $R_0 = 2.5\lambda_F$ (green), $R_0 = 3\lambda_F$ (blue), and $R_0 = 4\lambda_F$ (black).

sufficiently small values of length L_c and radius R_0 qualitatively recover the experimental data shown in Figure 3A, notably the exponential decay of the photon counts with the number of channels opened. We use the model described above to match the experimental dependence of the photon counts versus electrical power delivered in the contact displayed in Figure 3B, again considering the two extreme heat exchange scenarios at the side wall. The open blue and magenta triangles in Figure 3B are the results of the models considering a short cylinder of length $L_c = \lambda_F/4$ and $R_0 = 2\lambda_F$. We estimate the total radiation area as $S \approx \pi R_0^2 + 2\pi R_0 L_c = 4.84 \times 10^{-14}$ cm^2. The overall detection efficiency is experimentally unknown, and we leave this as a free parameter η. To fit the maximum calculated yield with the experimental value for the fourth

quantum channel, one should put $\eta \simeq 0.43$, which means that the collection efficiency of the microscope is about 43%. Considering the detection NA and the efficiency of the APDs in the spectral window, this value of η looks reasonable. The experimental photon counts are bounded by the two limiting cases of the model, indicating the qualitative agreement with the model used and that electron thermalization at the side wall is an important process to consider.

5 Conclusions

Past research in atomic-size point contacts has provided a firm understanding of the radio frequency electromagnetic response occurring when the system is driven in the linear regime of low bias voltages (e.g. in the mV range). Recent reports have suggested that electrons transported through the contact with a large kinetic energy (~eV) may unveil new nonlinear mechanisms of light emission. Our findings show that photons with energies much higher than the kinetic energy of the electron are emitted during the formation of the contact when the transport becomes ballistic. Our experiment has revealed that the number of photons collected exponentially increases when the quantized transport channels are closing. By assuming an electron distribution near the contact, which is no longer at equilibrium with the phonon population, we derived a model relating the electron temperature and the photon yield to the number of channels. We find that the out-of-equilibrium electron temperature distribution increases when quantum channels are closing during the electromigration process. Within this model, we assumed the presence of a small interconnection region between the quantum channel and the body of the drain contact, in which transport of hot electrons proceeds in a quasi-ballistic manner. Energy exchange in this interconnection region is mainly guided by electron collisions at the side wall rather than electron-phonon and electron-electron interactions. Hot electrons emit photons in an overbias spectral domain as a result of the Bremsstrahlung process driven by the boundary of the interconnection region. We derived (to our knowledge, for the first time) the quantum mechanical formula for the rate of this Bremsstrahlung photon emission, which in the limit $\hbar\omega \to 0$ coincides with the classical relation. We found qualitative agreement between the estimated emission rates and the results of our measurements. At that stage of the research, the dynamics leading to the formation of the contact remains too rapid to interrogate the spectrum of the emitted photons and their statistics. Once we have a reliable strategy to control the closing and opening of the electron transport channels, these findings will contribute to the development and engineering of integrated, electrically driven optical light sources at atomic length scales.

Acknowledgments: This work was funded by the European Research Council under the European Community's Seventh Framework program FP7/2007-2013 Grant Agreement 306772, Funder Id: http://dx.doi.org/10.13039/100011199, the CNRS/RFBR collaborative research program number 1493, Funder Id: http://dx.doi.org/10.13039/501100000921 (Grant RFBR-17-58-150007), the COST Action MP1403 "Nanoscale Quantum Optics" supported by COST (European Cooperation in Science and Technology), and the Regional Excellence funding scheme (project APEX). A.U. and I.S are thankful to the Russian Science Foundation (Grant 17-19-01532, Funder Id: http://dx.doi.org/10.13039/501100006769) for additional support. Access to the nanofabrication facility ARCEN Carnot was financed by the Regional council of Burgundy and la Délégation Régionale à la Recherche et à la Technologie (DRRT).

References

[1] Agraït N, Yeyati AL, van Ruitenbeek JM. Quantum properties of atomic-sized conductors. Phys Rep 2003;377:81–279.
[2] Cui L, Jeong W, Hur S, et al. Quantized thermal transport in single-atom junctions. Science 2017;355:1192–5.
[3] Datta S. Electronic transport in mesoscopic systems. Cambridge studies in semiconductor physics and microelectronic engineering. Cambridge, Cambridge University Press, 1995.
[4] van Houten H, Beenaker C. Quantum point contacts. Phys Today 1996;49:22.
[5] Green F, Das MP. Noise and transport in mesoscopics: physics beyond the landauer-büttiker formalism. Fluct Noise Lett 2005;5:C1–14.
[6] Das MP, Green F. Mesoscopic transport revisited. J Phys Condens Matter 2009;21:101001.
[7] Todorov TN. Local heating in ballistic atomic-scale contacts. Philos Mag B 1998;77:965–73.
[8] Agraït N, Untiedt C, Rubio-Bollinger G, Vieira S. Onset of energy dissipation in ballistic atomic wires. Phys Rev Lett 2002;88:216803.
[9] Frederiksen T, Brandbyge M, Lorente N, Jauho A-P. Inelastic scattering and local heating in atomic gold wires. Phys Rev Lett 2004;93:256601.
[10] Reznikov M, Heiblum M, Shtrikman H, Mahalu D. Temporal correlation of electrons: suppression of shot noise in a ballistic quantum point contact. Phys Rev Lett 1995;75:3340–3.
[11] Kumar M, Avriller R, Yeyati AL, van Ruitenbeek JM. Detection of vibration-mode scattering in electronic shot noise. Phys Rev Lett 2012;108:146602.

[12] Beenakker CJ, Schomerus H. Antibunched photons emitted by a quantum point contact out of equilibrium. Phys Rev Lett 2004;93:096801.
[13] Lebedev AV, Lesovik GB, Blatter G. Statistics of radiation emitted from a quantum point contact. Phys Rev B 2010;81:155421.
[14] Fulga IC, Hassler F, Beenakker CWJ. Nonzero temperature effects on antibunched photons emitted by a quantum point contact out of equilibrium. Phys Rev B 2010;81:115331.
[15] Zakka-Bajjani E, Dufouleur J, Coulombel N, Roche P, Glattli DC, Portier F. Experimental determination of the statistics of photons emitted by a tunnel junction. Phys Rev Lett 2010;104:206802.
[16] Forgues J-C, Gasse G, Lupien C, Reulet B. Non-classical radiation emission by a coherent conductor. C R Phys 2016;17:718–28. [Quantum microwaves/Micro-ondes quantiques.]
[17] Rogovin R, Scalapino DJ. Fluctuation phenomena in tunnel junctions. Ann Phys 1974;86:1–90.
[18] Février P, Gabelli J. Tunneling time probed by quantum shot noise. Nat Commun 2018;9:4940.
[19] Fedorovich R, Naumovets A, Tomchuk P. Electron and light emission from island metal films and generation of hot elctrons in nanoparticles. Phys Rep 2000;328:73–9.
[20] Green F, Thakur JS, Das MP. Where is the shot noise of a quantum point contact? Phys Rev Lett 2004;92:156804.
[21] D'Agosta R, Sai N, Di Ventra M. Local electron heating in nanoscale conductors. Nano Lett 2006;6:2935–8.
[22] Chen R, Wheeler PJ, Ventra MD, Natelson D. Enhanced noise at high bias in atomic-scale Au break junctions. Sci Rep 2014;4:4221.
[23] Park H, Lim AKL, Park J, Alivisato AP, McEuen PL. Fabrication of metallic electrodes with nanometer separation by electromigration. Appl Phys Lett 1999;75:301.
[24] Umeno A, Hirakawa K. Nonthermal origin of electromigration at gold nanojunctions in the ballistic regime. Appl Phys Lett 2009;94:162103.
[25] Trouwborst ML, van der Molen SJ, van Wees BJ. The role of joule heating in the formation of nanogaps by electromigration. J Appl Phys 2006;99:114316.
[26] Dasgupta A, Buret M, Cazier N, et al. Electromigrated electrical optical antennas for transducing electrons and photons at the nanoscale. Beilstein J Nanotechnol 2018;9:1964–76.
[27] Strachan D, Smith D, Johnston D, et al. Controlled fabrication of nanogaps in ambient environment for molecular electronics. Appl Phys Lett 2005;86:043109.
[28] Hoffmann R, Weissenberger D, Hawecker J, Stöffler D. Conductance of gold nanojunctions thinned by electromigration. Appl Phys Lett 2008;93:043118.
[29] Uskov AV, Khurgin JB, Buret M, Bouhelier A, Smetanin IV, Protsenko IE. Biased nanoscale contact as active element for electrically driven plasmonic nanoantenna. ACS Photon 2017;4:1501–5.
[30] O'Neill K, Osorio EA, van der Zant HSJ. Self-breaking in planar few-atom au constrictions for nanometer-spaced electrodes. Appl Phys Lett 2007;90:133109.
[31] Mangin A, Anthore A, Della Rocca ML, Boulat E, Lafarge P. Reduced work functions in gold electromigrated nanogaps. Phys Rev B 2009;80:235432.
[32] Muller CJ, van Ruitenbeek JM, de Jongh LJ. Conductance and supercurrent discontinuities in atomic-scale metallic constrictions of variable width. Phys Rev Lett 1992;69:140–3.
[33] Kizuka T, Kodama S, Matsuda T. Verification of unzipping models of electromigration in gold nanocontacts by in situ high-resolution transmission electron microscopy. Nanotechnology 2010;21:495706.
[34] de Heer W, Frank S, Ugarte D. Fractional quantum conductance in gold nanowires. Z Phy B Condens Matter 1997;104:469–73.
[35] Fujii A, Ichi Mizobata J, Kurokawa S, Sakai A. Stability of atom-sized metal contacts under high biases. e-J Surf Sci Nanotechnol 2004;2:125–30.
[36] Buret M, Uskov AV, Dellinger J, et al. Spontaneous hot-electron light emission from electron-fed optical antennas. Nano Lett 2015;15:5811–8.
[37] Lambe J, McCarthy SL. Light emission from inelastic electron tunneling. Phys Rev Lett 1976;37:923–5.
[38] Kern J, Kullock R, Prangsma JC, Emmerling M, Kamp M, Hecht B. Electrically-driven optical antennas. Nat Photon 2015;9:582–6.
[39] Parzefall M, Bharadwaj P, Jain A, Taniguchi T, Watanabe K, Novotny L. Antenna-coupled photon emission from hexagonal boron nitride tunnel junctions. Nat Nanotechnol 2015;10:1058.
[40] Qian H, Hsu S-W, Gurunatha K, et al. Efficient light generation from enhanced inelasticelectron tunnelling. Nat Photon 2018;12:485–8.
[41] Bigourdan F, Hugonin J-P, Marquier F, Sauvan C, Greffet J-J. Nanoantenna for electrical generation of surface plasmon polaritons. Phys Rev Lett 2016;116:106803.
[42] Uskov AV, Khurgin JB, Protsenko II, Smetanin IV, Bouhelier A. Excitation of plasmonic nanoantennas by nonresonant and resonant electron tunnelling. Nanoscale 2016;8:14573–9.
[43] Parzefall M, Szabó Á, Taniguchi T, Watanabe K, Luisier M, Novotny L. Light from van der waals quantum tunneling devices. Nat Commun 2019;10:292.
[44] Parzefall M, Bharadwaj P, Novotny L. Quantum plasmonics. In: Bozhevolnyi SI, Martin-Moreno L, Garcia-Vidal F, eds. Springer series in solid-state sciences, Vol. 185. Berlin Heidelberg, Germany, Springer, 2017:211–36.
[45] Malinowski T, Klein HR, Iazykov M, Dumas P. Infrared light emission from nano hot electron gas created in atomic point contacts. Europhys Lett 2016;114:57002.
[46] Schull G, Néel N, Johansson P, Berndt R. Electron-plasmon and electron-electron interactions at a single atom contact. Phys Rev Lett 2009;102:057401.
[47] Xu F, Holmqvist C, Belzig W. Ovembias light emission due to high-order quantum noise in a tunnel junction. Phys Rev Lett 2014;113:066801.
[48] Kaasbjerg K, Nitzan A. Theory of light emission from quantum noise in plasmonic contacts: above-threshold emission from higher-order electron-plasmon scattering. Phys Rev Lett 2015;114:126803.
[49] Peters P-J, Xu F, Kaasbjerg K, Rastelli G, Belzig W, Berndt R. Quantum coherent multielectron processes in an atomic scale contact. Phys Rev Lett 2017;119:066803.
[50] Ashcroft NW, Mermin ND. Solid state physics, 3rd ed. Philadelphia, PA, Saunders College, 1968.
[51] Kanavin AP, Smetanin IV, Isakov VA, et al. Heat transport in metals irradiated by ultrashort laser pulses. Phys Rev B 1998;57:14698–703.
[52] Belotskii ED, Tomchuk PM. Electron-phonon interaction and hot electrons in small metal islands. Surf Sci 1990;239:143–55.

[53] Kompaneets A. The establishment of thermal equilibrium between quanta and electrons. Sov Phys JETP 1957;4: 730–7.
[54] Zeldovich YB. Interaction of free electrons with electromagnetic radiation. Sov Phys Usp 1975;18:79–98.
[55] Chopra KL, Bobb LC, Francombe MH. Electrical resistivity of thin single crystal gold films. J Appl Phys 1963;34:1699–702.
[56] Ghisellini G. Radiative processes in high energy astrophysics. Lecture notes in physics. Heidelberg, Springer, 2013.
[57] Trivedi N, Ashcroft NW. Quantum size effects in transport properties of metallic films. Phys Rev B 1988;38:12298–309.
[58] Smet J, Fonstad C, Hu Q. Intrawell and interwell intersubband transitions in multiple quantum wells for far infrared sources. J Appl Phys 1996;79:9305.
[59] Nag B. Physics of quantum well devices. New York, Kluwer Academic Publishers, 2002.
[60] Landau L, Lifshitz E. The classical theory of fields, Vol. 2. Oxford, Pergamon Press, 1971.